Ward, J. A., Wilson, R. E., & Berg, P. K. (2007). Multiscale analysis of a spatially heterogeneous microscopic traffic model.

Multiscale Analysis of a Spatially Heterogeneous Microscopic Traffic Model

Jonathan Ward [a,*], R. Eddie Wilson [a], Peter Berg [b]

[a] *University of Bristol, Department of Engineering Mathematics, Bristol, BS8 1TR, United Kingdom*

[b] *UOIT, Faculty of Science, Oshawa, ON, L1H 7K4, Canada*

Abstract

The microscopic Optimal Velocity (OV) model is posed on an inhomogeneous ring-road, consisting of two spatial regimes which differ by a scaled OV function. Parameters are chosen throughout for which all uniform flows are linearly stable. The large-time behaviour of this discrete system is stationary and exhibits three types of macroscopic traffic pattern, each consisting of plateaus joined together by sharp interfaces. At a coarse level, these patterns are determined by simple flow and density balances, which in some cases have non-unique solutions. The theory of characteristics for the classical Lighthill-Whitham PDE model is then applied to explain which pattern the OV model selects. A global analysis of a second order PDE model is then performed in an attempt to explain some qualitative details of interface structure. Finally, the full microscopic model is analysed at the linear level to explain features which cannot be described by the present macroscopic approaches.

Key words: Traffic modelling; Multiscale analysis; Optimal Velocity model; Bottlenecks, Wave patterns; Phase-plane analysis
PACS: 05.45.-a, 45.50.-j, 47.40.-x, 47.54.-r

1 Introduction

Since the mid 1990s, there has been much interest in the spatio-temporal dynamics of highway traffic flow models (see [1–3]). In particular, Kerner and

* Corresponding author.
Email addresses: Jon.Ward@bristol.ac.uk (Jonathan Ward), RE.Wilson@bristol.ac.uk (R. Eddie Wilson), Peter.Berg@uoit.ca (Peter Berg).

collaborators [4] understood that the classical gas dynamics models developed by Lighthill, Whitham and Richards [5] could not capture all of the qualitative features in empirical data collected from inductance loop systems. Consequently, a major goal has been to develop better models with one objective being that they reproduce the so-called *spontaneous flow breakdown* effect, where small disturbances in the traffic may amplify in some circumstances to give large amplitude *stop-and-go* waves.

Intensive studies of such complex dynamics in a spatially uniform setting can be found in the applied mathematics and theoretical physics literature. In contrast, much less attention has been drawn to the fundamental mechanisms that explain wave solutions on a spatially heterogeneous highway, e.g. as a consequence of a changing speed limit, or a change in the number of lanes, a merge with an input road, or restrictions due to road works etc., although these are important scenarios from the point of view of practical applications. Furthermore, highway traffic data collected from inductance loops suggests that most spatio-temporal wave patterns are triggered by spatial inhomogeneities. Therefore, more detailed research is needed to understand traffic patterns caused by road heterogeneities.

In this paper, we analyse the wave structures of a highly simplified model of highway traffic, namely the microscopic Optimal Velocity (OV) model [6], in which vehicles are modelled as discrete entities moving in continuous time and space. The parameters are chosen so that uniform flows are stable. Consequently stop-and-go patterns are impossible, yet we force spatial patterns by introducing spatial heterogeneity in the form of a crude bottleneck model. In order to limit the variety of patterns that may form and to simplify the study, we analyse a ring road which forms a closed loop. This removes the need to prescribe an upstream boundary condition and also prohibits certain types of wave structure, e.g. expansion fans cannot persist as $t \to \infty$ since their up- and down-stream tails would eventually interact with each other. Our set-up is thus identical to the recent paper by Hanaura *et al.* [7], but our analysis goes further in that we extract a phase diagram from the resulting flow and density balances and we explain in detail the wave selection principles that were previously overlooked. Furthermore, the latter part of this paper is concerned with a detailed analysis of wave structure.

In what follows, we make use of the idea that the modelling of traffic flow can be understood at two distinct levels: microscopically, whereby each vehicle is considered individually, and macroscopically whereby traffic is considered as a continuous fluid. Often, these two approaches are treated independently. The key point of this paper, however, is that the simple discrete model that we consider here develops stable stationary patterns as $t \to \infty$, which can be understood by drawing parallels with continuum models.

The paper is set out as follows. In Section 2, we describe the OV model set-up, including precise details of how the spatial inhomogeneity is applied. Then we outline our numerical simulation and coarse-graining procedure, and we show results of three numerical experiments with qualitatively different solution structures as $t \to \infty$ (see Fig. 1). Sections 3 and 4 investigate these experiments using classical kinematic wave theory, firstly by analysing simple flow and density balances and then by using characteristic arguments to explain the wave selection principles. In Section 5, we investigate the structures of the various shock waves, using a travelling-wave phase-plane of a continuum (PDE) model that approximates the microscopic dynamics on a macroscopic scale [8]. In fact this method is insufficient in that it cannot explain all wave features and, therefore, a spectral analysis of the original microscopic model is carried out in Section 6. Finally in Section 7, we conclude and indicate the success and failures of higher order continuum models in explaining the fine details of the solution structure.

2 Problem Set-Up and Simulation Results

We consider the traffic patterns formed by a large number N of identical vehicles driving on a unidirectional single-lane ring-road of length L. Overtaking is not considered. Vehicles move in continuous space x and time t, and their displacements and velocities are labelled $x_n(t)$ and $v_n(t)$ respectively. We suppose that the direction of motion is in increasing x, and moreover that vehicles are labelled $n = 1, 2, \ldots, N$ in the downstream direction. For the vehicles' equations of motion, we adopt the well-known Optimal Velocity (OV) car-following model [6] for which

$$\dot{x}_n = v_n, \tag{1}$$
$$\dot{v}_n = \alpha \left\{ V(h_n; x) - v_n \right\}. \tag{2}$$

Here dot denotes differentiation with respect to time, and the rate constant $\alpha > 0$ is known as the sensitivity. The variable $h_n := x_{n+1} - x_n$ gives the headway, or gap to the vehicle in front, and loosely speaking the OV model describes the relaxation of traffic to a safe speed which is defined in terms of this gap. Note that under open boundary conditions one would need to prescribe the trajectory of the lead vehicle N, but on the ring-road we assume merely that it follows vehicle 1, so that $h_N = L + x_1 - x_N$.

The inhomogeneous OV function that we use here takes the form

$$V(h_n; x) := \begin{cases} r_{\mathrm{B}} V(h_n), & 0 \le x \bmod L < \hat{L} L, \\ V(h_n), & \hat{L} L \le x \bmod L < L, \end{cases} \tag{3}$$

and which is thus scaled down by a reduction factor $0 < r_{\rm B} < 1$ for a proportion $0 < \hat{L} < 1$ of the ring-road under consideration. Note that for the sake of simplicity, the vehicles' displacements $x_n(t)$ are set-up as monotone increasing and unbounded, although henceforth we interpret all results modulo L.

In (3), V with a single argument denotes a spatially independent OV function, and for concreteness, we adopt the standard [6] S-shape

$$V(h) = \tanh(h-2) + \tanh(2). \tag{4}$$

However, qualitatively similar results should be recovered by any V for which 1. $V(0) = 0$, 2. $V' \geq 0$ and 3. $V(h) \to V_{\max}$ as $h \to \infty$, and for which the flow is linearly stable. Therefore, throughout this paper we choose $\alpha \geq 2\,\max V'(h)$, thereby ensuring linear stability [6]. Consequently, the patterns that we observe are forced only by spatial inhomogeneity and not by spontaneous flow breakdown effects.

Next we supplement Eqs. (1–3) with the uniformly spaced initial data

$$x_n = nh_* \quad \text{and} \quad v_n = V(h^*) \quad \text{for } n = 1, 2, \ldots, N. \tag{5}$$

Here $h^* := L/N$ is the mean spacing. Note that for the limiting (no bottleneck) cases where either $r_{\rm B} = 1$ or $\hat{L} = 0$, (5) gives a uniform flow solution of (1)–(3) in which $x_n = nh_* + tV(h^*)$. However, in general we should expect the bottleneck to redistribute traffic. In order to investigate the resulting patterns, we solve the initial value problem (1–5) numerically using a standard fixed step fourth-order Runge-Kutta solver.

After extensive experimentation with the solver, we conclude that the traffic always settles down to a stationary profile as $t \to \infty$, although the transient processes can sometimes be very long. Here stationarity means that suitably defined macroscopic density and velocity variables become steady, although they are non-trivially dependent on space x. Consequently vehicles' motions are in fact periodic as $t \to \infty$, since as they drive around the ring-road, they move repeatedly through the spatial pattern and experience traffic jams, free-flowing regimes etc. Note however that if we chose smaller values of sensitivity α than presented here, so as to force the linear instability of a range of uniform flows, then the macroscopic variables could also be non-trivially time-dependent as $t \to \infty$.

Taking into account the above discussion, the results that we display shortly show stationary macroscopic density profiles $\rho(x)$ rather than individual vehicle trajectories. The simplest way to relate microscopic and macroscopic variables is via $\rho(x_n, t) = 1/h_n(t)$, although it is well-known [8,9] that this relationship holds exactly only for equilibrium situations. Therefore we use a coarse-grained

density [8] which is obtained from the distributional point density by convolving with a normalised Gaussian test function whose characteristic length scale is chosen large enough so as to smooth out individual vehicles but small enough so as to retain macroscopic features. A macroscopic flow variable $q(x,t)$ may be obtained in a similar way by coarse-graining the discrete velocity v_n, and then a coarse-grained velocity is given by $v(x,t) := q(x,t)/\rho(x,t)$. However, flows are stationary in our study. Hence it proves sufficient to coarse-grain the trajectory data of a single vehicle with a temporal kernel only, thus providing a substantial simplification of the general case presented in [8]. Moreover, since the time step in the initial value solver may be chosen as small as we wish, any macroscopic feature can be adequately resolved by this approach.

We now give three examples of the eventual stationary profiles $\rho(x)$ which show how the structure changes as the mean headway h^* is varied. To simplify matters, all other parameters are held fixed as follows: $N = 100$ vehicles, bottleneck reduction factor $r_{\rm B} = 0.6$, bottleneck nondimensionalised length $\hat{L} = 0.25$ and sensitivity $\alpha = 3.0$. We should emphasise that the resulting structures, shown in Fig. 1, have been found in earlier papers [10,7]. The novel feature here is that we analyse in detail how the qualitative solution structures change as functions of the three problem parameters $\rho_* := 1/h_*$, $r_{\rm B}$ and $\hat{L}$.

Example 1. We take $h_* = 7.0$ which corresponds to light traffic (large h_*, small ρ_*), shown in Fig. 1(a). The $t \to \infty$ steady density profile $\rho(x)$ adopts a two-plateau form, with an almost constant density $\rho_{\rm B} \approx 0.12$ attained in the bottleneck and a lower (almost constant) density $\rho_1 \approx 0.20$ on the remainder of the loop. At each end of the bottleneck, the two density plateaus are joined by sharp, almost shock-like fronts.

Example 2. We take $h_* = 1.0$ which corresponds to heavy traffic, exhibited in Fig. 1(c). In a similar fashion to Example 1, $\rho(x)$ adopts a two-plateau form. However this time the bottleneck density $\rho_{\rm B} \approx 0.71$ is less than the density $\rho_1 \approx 1.09$ on the unconstrained part of the loop. Like Example 1, there are also sharp, shock-like fronts at each end of the bottleneck, although here they have a more complicated oscillatory structure.

Example 3. We now take $h_* = 2.5$ which may be regarded as an intermediate case, presented in Fig. 1(b). In contrast to the two previous examples, $\rho(x)$ now has a three-plateau form. The density as before adopts an almost constant (but slightly S-shaped) profile $\rho \simeq 0.36$ within the bottleneck, with fronts at each end. Downstream of the bottleneck is a low density $\rho_1 \approx 0.17$ region, whereas upstream is a high density $\rho_2 \approx 0.64$ region, which may be thought of as a queue waiting to enter the bottleneck. There is thus an extra internal shock-like front in the unconstrained part of the loop, where the fast traffic

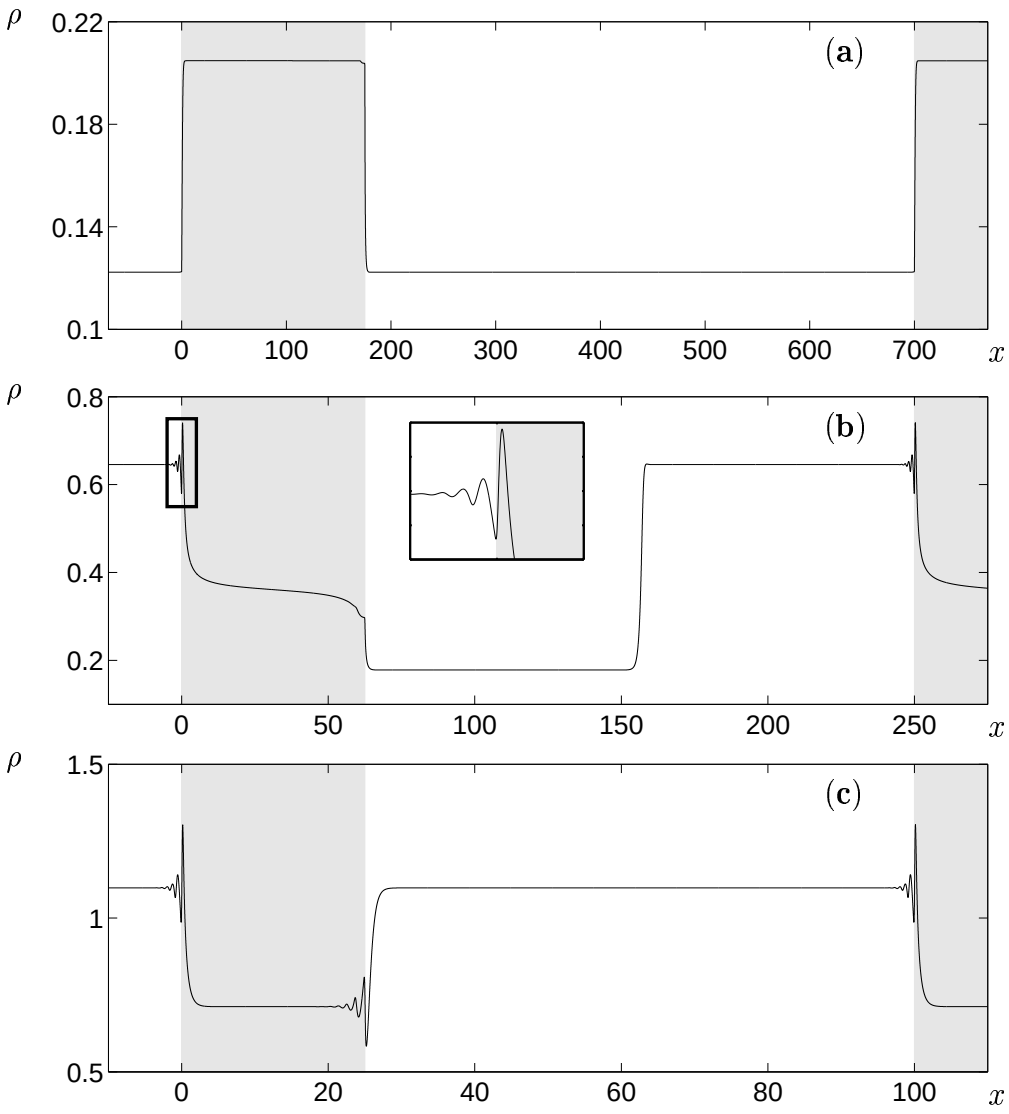

Fig. 1. Stationary $t \to \infty$ coarse-grained density profiles $\rho(x)$. The portions of solution profiles within the bottleneck are indicated by shading. (a) Light traffic $h_* = 7.0$ ($\rho_* = 0.142857$), see Example 1; (b) Medium traffic $h_* = 2.5$ ($\rho_* = 0.4$), see Example 3; (c) Heavy traffic $h_* = 1.0$ ($\rho_* = 1.0$), see Example 2.

that emerges from the bottleneck rejoins the queue to enter it. Unlike the other fronts we have encountered so far, the wave joining ρ_1 and ρ_2 is not locked onto a discontinuity in the model; nevertheless, it is stationary.

Further simulation may be used to show how the Fig. 1 profiles are related to each other. If one starts with the Fig. 1(b) structure (Example 3) and decreases the mean headway (increases the mean density), then the queue upstream of the bottleneck grows in length until it reaches the downstream boundary of the bottleneck, and swamps the entire unconstrained part of the loop. At this point, the internal shock vanishes and the Fig. 1(c) structure is recovered. Conversely, if one starts with Fig. 1(b) and decreases the mean density, the

queue upstream of the bottleneck shortens until it vanishes altogether. At that point, the internal shock is absorbed into the upstream boundary of the bottleneck and the Fig. 1(a) structure is recovered.

3 Density and Flow Balances

We now begin an explanation of the structures seen in Section 2. Later we derive a phase diagram which predicts when each will occur. Since the observed structures resemble constant density plateaus separated by classical shocks, we initially attempt an explanation based on kinematic wave theory [5]. To this end, we introduce the fundamental (flow) diagram $Q(\rho) = \rho\hat{V}(\rho)$ where $\hat{V}(\rho) = V(1/\rho)$ is the continuum counterpart to the discrete OV function V. As is well-known, Q is usually a unimodal function. With choice (4), Q attains its maximum value $Q_{\max} \simeq 0.58$ at $\rho_{\max} \simeq 0.36$. In the bottleneck, the fundamental diagram Q is scaled by r_{B}.

Firstly we consider the two-plateau structures of Fig. 1(a) and (c). Since the fronts are sharp, negligibly few vehicles are contained within them at any one time. We may therefore approximate the density $\rho(x)$ with a piecewise-constant profile consisting of ρ_{B} within the bottleneck and ρ_1 in the unconstrained part of the loop. It thus follows that

$$\hat{L}\rho_{\mathrm{B}} + (1-\hat{L})\rho_1 = \rho_*, \tag{6}$$

$$Q(\rho_1) = r_{\mathrm{B}} Q(\rho_{\mathrm{B}}), \tag{7}$$

which describe respectively the conservation of vehicles and a flow balance (the latter is necessary since the observed profiles are stationary). Eqs. (6,7) are thus a pair of simultaneous equations to solve for ρ_1 and ρ_{B}, where the remaining parameters ρ_*, r_{B} and $\hat{L}$ are prescribed.

We must therefore examine the $(\rho_1, \rho_{\mathrm{B}})$ solution structure of (6,7) and this is achieved via Fig. 2. To see this, note that ρ_{B} may be eliminated from (6,7) to give

$$Q(\rho_1) = r_{\mathrm{B}} Q\left(\frac{\rho_* - (1-\hat{L})\rho_1}{\hat{L}}\right), \tag{8}$$

and the left and right hand sides of this equation are plotted against ρ_1 in Fig. 2(a-c)(i). Note alternatively that ρ_1 can be eliminated from (6,7) to give

$$r_{\mathrm{B}} Q(\rho_{\mathrm{B}}) = Q\left(\frac{\rho_* - \hat{L}\rho_{\mathrm{B}}}{1-\hat{L}}\right), \tag{9}$$

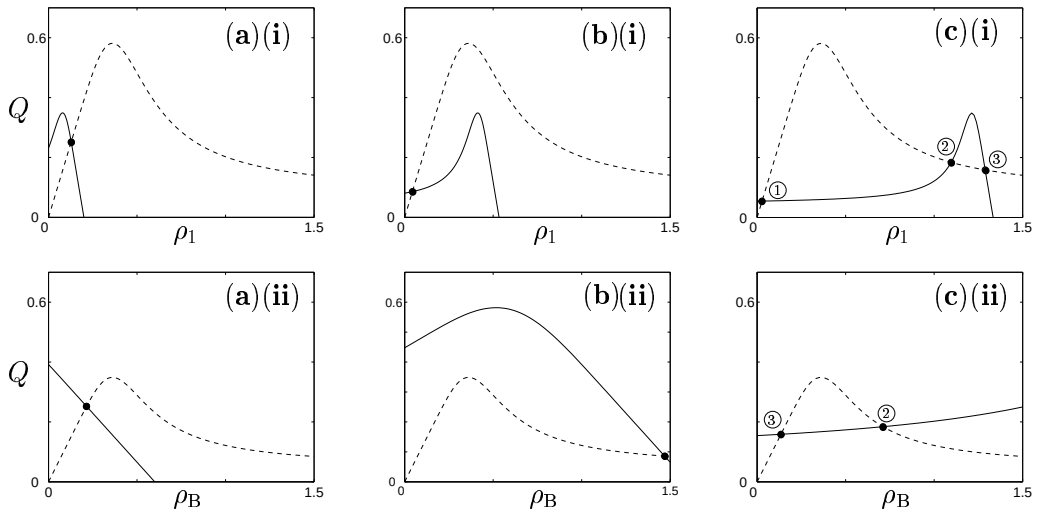

Fig. 2. Solution structure of (6,7). Panels (a-c) correspond directly to panels (a-c) in Fig. 1. Top row (i) indicates solutions of (8) and bottom row (ii) of Eq. (9). The extra numbering in panels (c)(i,ii) allows the (ρ_1, ρ_B) solution pairs to be identified.

and as a cross-check, the left and right hand sides of this equation are plotted against ρ_B in Fig. 2(a-c)(ii). Further, parameters have been chosen so that the panels (a-c) correspond directly to panels (a-c) in Fig. 1. Firstly, the light traffic diagrams Fig. 2(a)(i,ii) indicate a unique (ρ_1, ρ_B) solution pair and it may be shown that this is indeed corresponds to values obtained in Example 1.

However, in the heavy traffic diagrams Fig. 2(c)(i,ii), there are clearly three (ρ_1, ρ_B) solution pairs: what determines which pair is selected in the corresponding Example 2? Finally, in the intermediate case of Fig. 2(b)(i,ii), there is a unique (ρ_1, ρ_B) solution pair, however, the corresponding Example 3 selects instead a three-plateau structure. It now remains to identify extra principles which explain the solution selection in cases (b) (Example 3) and (c) (Example 2).

4 Wave Selection via Characteristics

We now use characteristic arguments from kinematic wave theory [5, Chap. 2] to explain the observed wave selection behaviour. We focus initially on Example 2 (heavy traffic), see Fig. 1(c) and Fig. 2(c)(i,ii), and then later we consider the three-plateau case.

We recall that in kinematic wave theory, characteristics are lines (or line segments) in the (x, t) plane on which density is conserved. Further, it is well-known that the local velocity of a characteristic with density ρ is given by $Q'(\rho)$. Consequently, characteristics propagate downstream in light traffic and

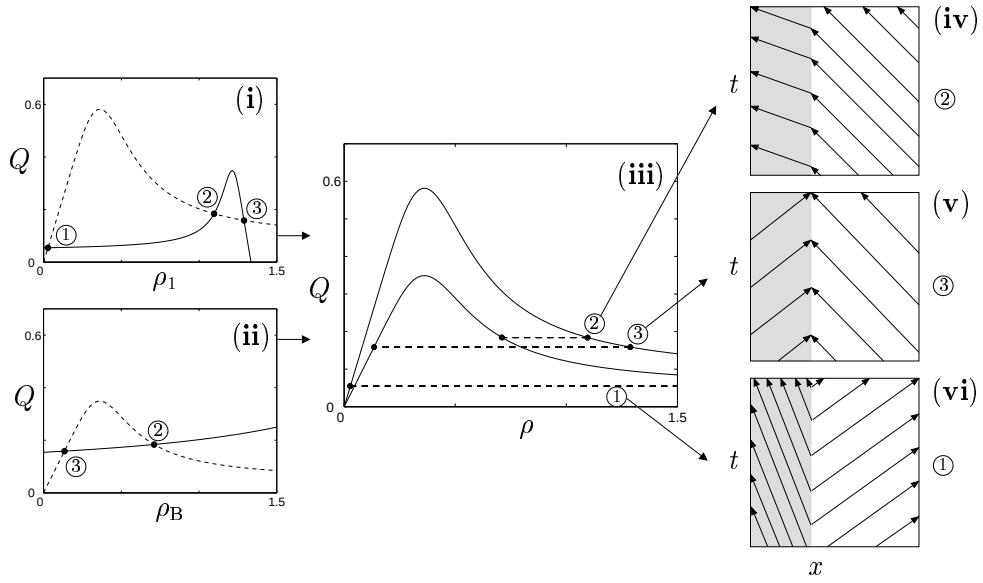

Fig. 3. Characteristic analysis for the (ρ_1, ρ_B) solution pairs from Fig. 2(c)(i,ii). Panel (iii) shows the location of solution pairs (pair (1) is not fully contained in the figure), joined by horizontal lines representing flow balance, on the fundamental diagrams Q and $r_B Q$. Characteristic pictures for each of the three root pairs are shown in panels (iv), (v) and (vi): the bottleneck is denoted by shading. Panels (v) and (vi) cannot give stationary profiles since they predict an expansion fan at the up- and down-stream ends of the bottleneck respectively. Hence solution pair 2 from panel (iv) is selected. Note that in panel (iii), this solution pair is non-straddling in the sense that both ρ_1 and ρ_B are the same side of the fundamental diagram maximum.

upstream in heavy traffic. When characteristics converge, one obtains a classical shock, whereas when they diverge, one obtains a (non-stationary) expansion fan.

Fig. 3 develops a characteristic analysis of the (ρ_1, ρ_B) solution pairs found in Fig. 2(c)(i,ii). The key point to note is that the solution pairs numbered 1 and 3 straddle $\rho = \rho_{max}$ at which both the unconstrained $Q(\rho)$ and bottleneck $r_B Q(\rho)$ fundamental diagrams attain their maxima. These solution pairs can be disregarded, because the consequent density profiles would involve patterns of characteristics with both positive and negative slopes. This means that at either the upstream or downstream boundary of the bottleneck, there would necessarily be a non-stationary expansion fan which would not agree with the $t \to \infty$ stationary results.

In contrast, solution pair 2 is non-straddling and involves only characteristics with negative slopes, see Fig. 3 panel (iv). In this sketch, neither the upstream or downstream boundary of the bottleneck has a classical (compressive) shock. Rather, at each boundary the characteristics cross through the shock which is forced solely by the model discontinuity at that point. It may be shown

that this solution agrees with that found by discrete simulation in Section 2 and moreover that it is a proper solution of the Lighthill-Whitham-Richards model in that it may be reached via the solution of the initial value problem [11].

We now turn our attention to the three-plateau case (Example 3, Fig. 1(b)), for which it may be shown that the analysis of Section 3 predicts a straddling, and hence invalid solution pair $(\rho_1, \rho_{\mathrm{B}})$. The resolution is thus to approximate the density $\rho(x)$ by a piecewise-constant profile with three components: ρ_{B} (density in bottleneck) and ρ_1, ρ_2 (densities in unconstrained part of loop). The density and flow balances thus yield respectively

$$\hat{L}\rho_{\mathrm{B}} + \beta(1-\hat{L})\rho_1 + (1-\beta)(1-\hat{L})\rho_2 = \rho_*, \tag{10}$$

$$Q(\rho_1) = Q(\rho_2) = r_{\mathrm{B}} Q(\rho_{\mathrm{B}}), \tag{11}$$

where $0 < \beta < 1$ parametrises the internal shock position separating ρ_1 and ρ_2. We thus have three equations, but four unknowns, namely β, ρ_1, ρ_2 and ρ_{B}, and we require extra information to fix a unique solution.

By studying characteristic diagrams, it becomes clear that a solution without diverging characteristics (and hence non-stationary expansion fans) is only possible if

$$\rho_{\mathrm{B}} = \rho_{\max}, \tag{12}$$

i.e., if the flow inside the bottleneck is maximised. Further, when supplemented by (12), system (10,11) can be solved uniquely for ρ_1, ρ_2 and β, and it may be shown that this solution agrees with the discrete simulations. The characteristic structure is shown in Fig. 4. In particular, it involves non-standard waves at the up- and down-stream ends of the bottleneck. However it may be shown via the solution of the initial value problem that these are admissible solutions of the Lighthill-Whitham-Richards model [11].

We now turn our attention to the computation of a phase diagram. Since in the three-plateau case we have $\rho_{\mathrm{B}} = \rho_{\max}$, the values of ρ_* where solutions change from two plateau solutions to three plateau solutions can be calculated. At the thresholds, β is either 0 or 1 and $\rho_{\mathrm{B}} = \rho_{\max}$, thus eliminating ρ_1 or ρ_2 in (11) using (10), leaves only

$$r_{\mathrm{B}} Q(\rho_{\max}) = Q\left(\frac{\rho_* - \hat{L}\rho_{\max}}{1-\hat{L}}\right), \tag{13}$$

as a relation between the problem parameters that holds at the transition, see Fig. 5. In particular, we may partition the (ρ_*, r_{B}) plane according to whether

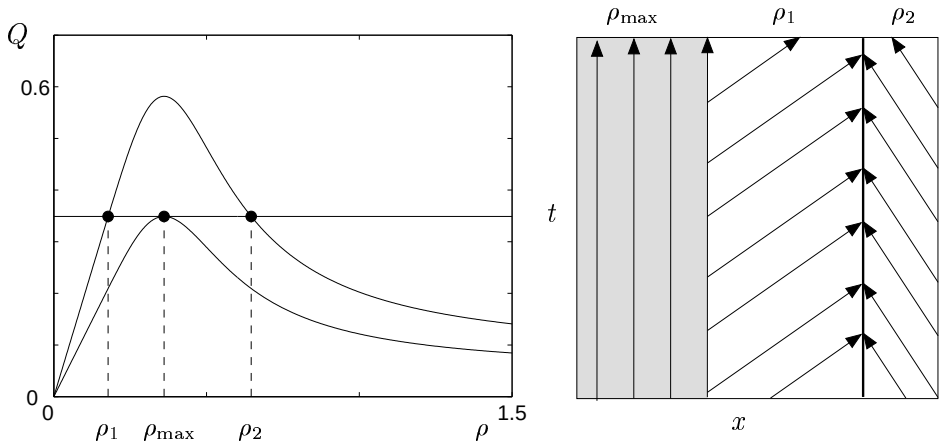

Fig. 4. Characteristic analysis for the three-plateau case: only the configuration shown with flow maximised in the bottleneck avoids expansion fans. Note that the characteristics inside the bottleneck have zero velocity and hence this structure is on the very boundary of becoming an expansion fan. The internal shock between ρ_1 and ρ_0 is classical since at it the characteristics converge.

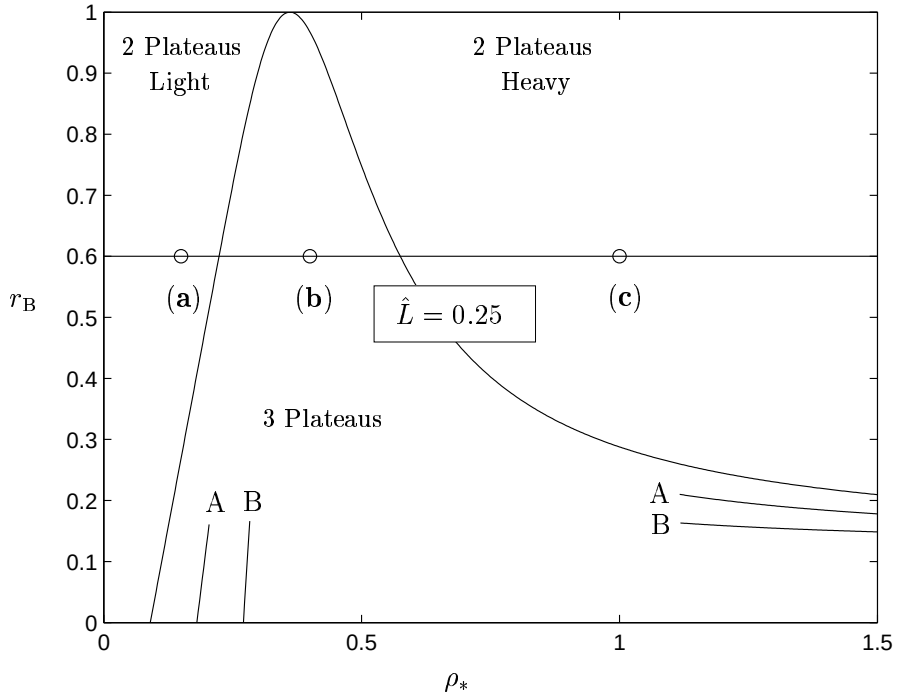

Fig. 5. Phase diagram derived from (13) for bottleneck length $\hat{L} = 0.25$. The points marked (a), (b), and (c) correspond to panels (a), (b) and (c) in Fig. 1 and Fig. 2. The line segments denoted A and B indicate to where the phase boundary would move for $\hat{L} = 0.5$ and $\hat{L} = 0.75$ respectively.

the three-plateau solution occurs, or according to which type of two-plateau solution occurs, and the boundary in this plane depends on $\hat{L}$ in a manner that we can determine explicitly. In particular, increasing the length of the bottleneck shrinks the domain where the three-plateau solution occurs.

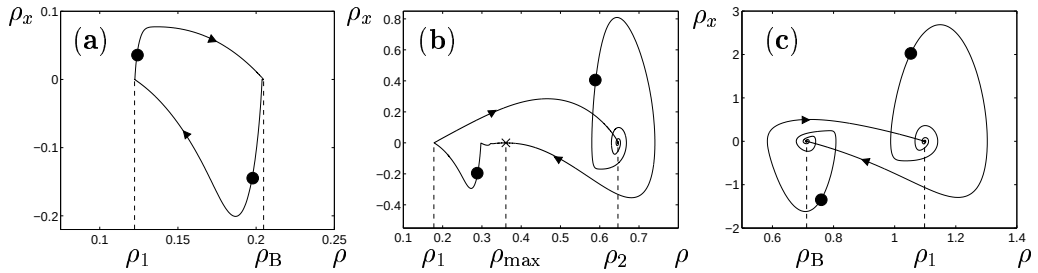

Fig. 6. Numerical (ρ,ρ_x) phase plots corresponding to Fig. 1(a-c). The discs mark the boundaries of the bottleneck. (a) Light traffic: heteroclinic cycle connecting $(\rho_1, 0)$ and $(\rho_B, 0)$. (b) Three plateau case: saddle at $(\rho_1, 0)$; saddle-node at $(\rho_{max}, 0)$ explaining S-shaped structure; complex fixed point at $(\rho_2, 0)$. (c) Heavy traffic: complex fixed points at $(\rho_1, 0)$ and $(\rho_B, 0)$.

5 Second Order Modelling

We have shown in Sections 3–4 how a first order kinematic wave theory approximation explains the plateau-like features of Fig. 1, in terms of piecewise constant profiles connected together by perfect discontinuities. However, the displacements and velocities arising from (1–3) are continuous, even at the bottleneck boundary, and moreover smoothing is involved in the coarse-graining process. Hence the fronts that connect plateaus are in fact continuous, and we now turn our attention to their structure. The main challenge is to examine whether a higher order macroscopic theory can explain the interface structure in the coarse-grained solution profiles, or whether it is necessary to analyse the microscopic model (1–3) directly.

In summary, our answer is that some features can be explained by second order PDE modelling (this section), whereas other features, that would not occur on a homogeneous road but which are forced directly by the bottleneck discontinuity, have such short wavelength that only an examination of the spectrum of (1,2) can explain them (see Section 6).

To focus this discussion, we are interested specifically in whether fronts are monotone (as in Fig. 1(a)), or whether they involve rapid oscillations (e.g., the upstream bottleneck boundary in Fig. 1(b) and both bottleneck boundaries in Fig. 1(c)). We would also like to explain the apparently S-shaped plateau in the bottleneck density profile of Fig. 1(b).

To emphasise these features, we re-map the coarse-grained data used to produce Fig. 1 into a (ρ, ρ_x) phase-plane, where ρ_x is obtained by numerical differentiation. The corresponding new figures are shown in Fig. 6(a-c). These diagrams are sometimes referred to as Poincaré phase-planes. The advantage of these coordinates is that almost-constant solution behaviour along a plateau is compressed into the neighbourhood of so-called *fixed points* ($(\rho_1, 0)$ and

$(\rho_B, 0)$ in Fig. 6(a) and 6(c), and $(\rho_1, 0)$, $(\rho_{\max}, 0)$ and $(\rho_2, 0)$ in Fig. 6(b)), whereas the sharp transitions between plateaus are stretched out. In particular, the rapid oscillations from Fig. 1 now express themselves in the form of spiralling features. A disadvantage of these coordinates is that the point of discontinuity in the model is now hidden; consequently we add solid discs to Fig. 6 to mark the points on the solution trajectories where the bottleneck boundaries are crossed.

Here we attempt to explain the structures in Fig. 6 using a macroscopic theory developed by Kim, Lee and Lee [8] (see also Berg, Mason and Woods [9] for a similar theory based on perturbation expansions). Their analysis shows that, in the long-wavelength near-equilibrium limit, the coarse-grained density $\rho(x,t)$ and velocity $v(x,t)$ arising from the Optimal Velocity model are approximate solutions of the PDE system

$$\rho_t + (\rho v)_x = 0, \tag{14}$$

$$v_t + v v_x = \alpha \left\{ \hat{V}(\rho) - v \right\} + \alpha \left[\hat{V}'(\rho) \frac{\rho_x}{2\rho} + \frac{v_{xx}}{6\rho^2} \right], \tag{15}$$

which resembles the Kerner-Konhäuser model [4], in that it consists of a conservation equation and a momentum equation, the latter being composed of an Optimal Velocity relaxation term plus a balance of pressure and diffusion effects. Here (14,15) must be generalised later to allow for spatial heterogeneity by making $\hat{V}$ and $\hat{V}'$ depend explicitly on x.

We now follow [12] by seeking steady solutions

$$v = W(x) \quad \text{and} \quad \rho = X(x), \tag{16}$$

to reduce (14,15) to an ordinary differential equation problem. The continuity equation (14) thus becomes $(WX)' = 0$, where $'$ denotes differentiation with respect to x. Direct integration then gives

$$W = q/X, \tag{17}$$

where q is an integration constant that equals the (spatially uniform, time-independent) flow around the ring. For example, if we are interested in solutions involving a non-bottleneck plateau with $\rho = \rho_1$, then $q = Q(\rho_1) = \rho_1 \hat{V}(\rho_1)$. Note that in [12], this argument is worked through with the travelling wave ansatz $v = W(z)$, $\rho = X(z)$ and $z = x - ct$, when one obtains the standard Rankine-Hugoniot result; that is, wave speed c is given by the gradient of a chord cutting the so-called fundamental diagram $Q(\rho)$, and furthermore that q is given by the intercept of this chord with the vertical Q axis.

By using (17), the velocity variable W can be eliminated from (15), resulting in a second order ODE in terms of the density variable X. This may be re-cast as the first order system

$$X' = Y, \tag{18}$$

$$Y' = \frac{6X^3}{q}\left[\frac{q^2 Y}{\alpha X^2} + \{Q(X;x) - q\}\right] + \left[\frac{2Y}{X} + \frac{3X^3 \hat{V}'(X;x)}{q}\right] Y. \tag{19}$$

The subtlety here is the spatial inhomogeneity due to the bottleneck, which makes (19) depend explicitly on space x. Thus Eqs. (18,19) actually represent a pair of phase-plane problems, one (unconstrained flow) in which

$$Q(X;x) = Q(X) \quad \text{and} \quad \hat{V}'(X;x) = \hat{V}'(X), \tag{20}$$

and one (bottleneck case) in which

$$Q(X;x) = r_{\mathrm{B}} Q(X) \quad \text{and} \quad \hat{V}'(X;x) = r_{\mathrm{B}} \hat{V}'(X). \tag{21}$$

Note that X', $Y' = 0$ fixed points correspond to plateaus. For such we require $Y = 0$ from (18), with (19) imposing the natural constraint $Q(X;x) = q$. Therefore the density values of plateaus are found by horizontal sections through the $Q(\rho)$ curve and all is consistent with Section 3. Furthermore, each of the (18,19,20) and (18,19,21) phase-planes typically has two fixed points $(\rho_{\mathrm{l}}, 0)$ and $(\rho_{\mathrm{r}}, 0)$ where ρ_{l} and ρ_{r} are respectively to the left and right of the maximum of Q at $\rho = \rho_{\max}$.

We now overlay the phase-planes for each of the cases (18,19,20) and (18,19,21), and seek paths which continuously combine segments of trajectories so as to connect up the required fixed points in accord with the selection principles established in Section 4. Fig. 7 illustrates how the procedure works. The reduction factor $r_{\mathrm{B}} = 0.6$ has been chosen to match Example 1 and q has been set equal to the resulting flow value $q = Q(\rho_1) = r_{\mathrm{B}} Q(\rho_{\mathrm{B}})$. See also Fig. 1(a) and Fig. 6(a). Fig. 7(a,b) plots numerical solution trajectories for systems (18,19,20) and (18,19,21) respectively, whose left- and right-hand fixed points are denoted $(\rho_{\mathrm{fl}}, 0)$, $(\rho_{\mathrm{fr}}, 0)$ and $(\rho_{\mathrm{bl}}, 0)$, $(\rho_{\mathrm{br}}, 0)$. The selection principles of Section 4 require plateaus whose densities do not straddle the maximum point of Q. Here this means that we seek a connection from $(\rho_{\mathrm{fl}}, 0)$ in the uncongested phase-plane to $(\rho_{\mathrm{bl}}, 0)$ in the bottleneck phase-plane. Thus Fig. 7(c) overlays Fig. 7(a,b) and magnifies the region of interest.

The goal of the overlay process is to use Fig. 7(c) to explain the structure of the discrete simulation result Fig. 6(a) which we reproduce in Fig. 7(d) in order to aid the comparison. At the qualitative level, there is excellent agreement and thus we may interpret the overall structure of Fig. 7(d) as

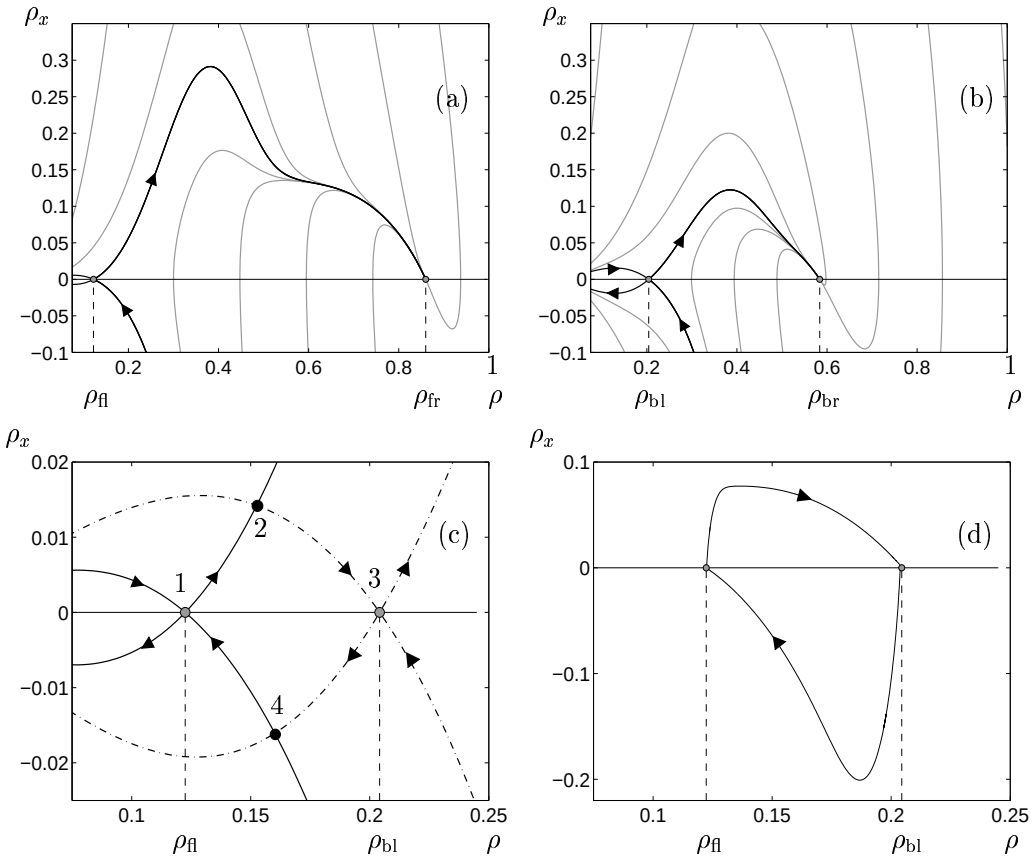

Fig. 7. Light traffic phase-plane topologies for (18,19), with parameters chosen so as to agree with Experient 1. (a) Unconstrained regime (20) and (b) bottleneck (21). Flows in the top half-plane go from left to right and flows in the bottom half-plane go from right to left. Dark lines indicate the manifolds associated with the saddle points at $(\rho_{\mathrm{fl}}, 0)$ and $(\rho_{\mathrm{bl}}, 0)$. The unstable manifolds connect through the upper half-plane with stable nodes at $(\rho_{\mathrm{fr}}, 0)$ and $(\rho_{\mathrm{br}}, 0)$. (c) Overlay of the separatrices from (a) and (b). Grey markers denote the fixed points and black markers denote where the seperatrices meet and hence where the switch between model (20) and model (21) occurs. Compare with (d) which is a reproduction of Fig. 1(b).

a heteroclinic cycle. Furthermore, the simple saddle-like nature of the states that are connected (which we explain shortly using linear theory), explains the monotone front structure of the density profile in Fig. 1(a). However, at the quantitative level, the comparison fails, as may be seen by comparing the vertical scale of Fig. 7(c,d). In practice, the coarse-grained density ρ_x achieves much larger values than the solutions of the PDE model (14,15). This should not come as a surprise, since the shock-like structures which we describe break the small amplitude, long wavelength premise on which the PDE derivation is based.

As we have indicated, further insight may be obtained via the linearisation

about fixed points of (18,19), see [12], where the Jacobian takes the form

$$J = \begin{pmatrix} 0 & 1 \\ g_x & g_y \end{pmatrix}, \tag{22}$$

and

$$g_x := \left.\frac{\partial Y'}{\partial X}\right|_{(X,0)} = \frac{6X^2}{\hat{V}(X)} Q'(X), \tag{23}$$

$$g_y := \left.\frac{\partial Y'}{\partial Y}\right|_{(X,0)} = \frac{3X^2}{\alpha \hat{V}(X)} \left(2\hat{V}(X)^2 + \alpha V'(X)\right). \tag{24}$$

The classification of fixed points is then governed by the eigenvalues of J, and in particular by the trace g_y and the determinant $-g_x$.

Firstly note for light traffic fixed points where $X < \rho_{\max}$, we have $Q'(X) > 0$ and consequently $g_x > 0$. Since the determinant is negative, such fixed points are saddles (e.g., the points $(\rho_{\mathrm{fl}}, 0)$ and $(\rho_{\mathrm{bl}}, 0)$ in Fig. 7).

For heavy traffic fixed points where $X > \rho_{\max}$, we have $Q'(X) < 0$ and consequently $g_x < 0$. Since the determinant is positive, the sign of the trace affects the classification. However, recall that here we operate solely in the stable regime where $\alpha > 2V'(h_*)$ and for such it may be shown that $g_y < 0$. The upshot is that such fixed points are either stable nodes or stable spirals in the (18,19) phase-plane (e.g., $(\rho_{\mathrm{fr}}, 0)$ and $(\rho_{\mathrm{br}}, 0)$ in Fig. 7) depending on how exactly other parameters are chosen.

We now use the PDE-based phase-plane argument to explain the bottleneck solution profile for the three-plateau structure of Example 2 (see Fig. 1(b) and Fig. 6(b)). Fig. 8(a) reproduces the coarse-grained simulation data of Fig. 6(b) with the bottleck section highlighted in bold, which is then overlaid with numerical solution trajectories of the bottleneck phase-plane (18,19,21) in Fig. 8(b). Since there is excellent agreement in the neighbourhood of the fixed point, we may use the linearisation to explain the structure there. We have $\rho_{\mathrm{sn}} = \rho_{\max}$, and thus the critical condition $Q'(\rho_{\mathrm{sn}}) = 0$ holds. Consequently, $(\rho_{\mathrm{sn}}, 0)$ is a degenerate fixed point of (18,19,21) which corresponds to the coalescence of fixed points of saddle and stable node type (see [13, Chap. 3.3]). In the neighbourhood of such a point, the variation in terms of the removed variable x is polynomial rather than exponential. Hence equilibriation on to the plateau is slow, explaining the pronounced S-shape in the bottleneck profile in Fig. 1(b).

Finally, we consider the qualitative limitations of the phase-plane argument

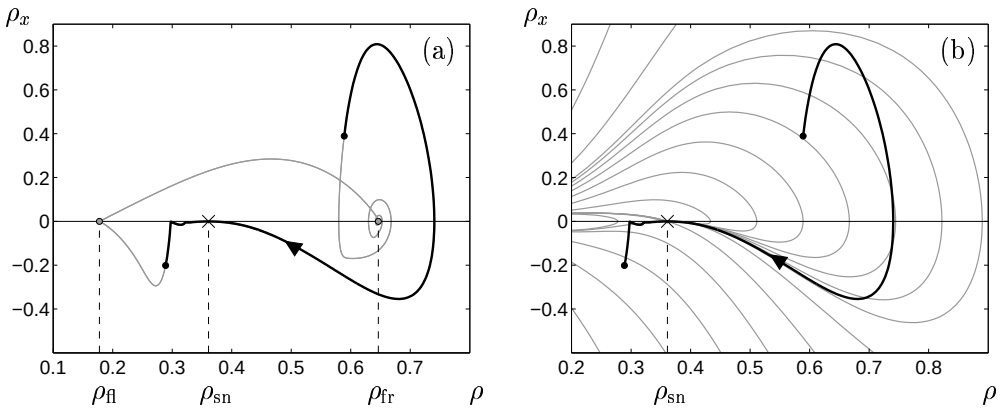

Fig. 8. (a) Reproduction of Fig. 6(b) where the portion of the trajectory corresponding to the bottleneck is highlighted in bold. (b) Overlay of (18,19,21) phase-plane trajectories (grey lines) with microscopic simulation data for the bottleneck from (a). The saddle node $(\rho_{\mathrm{sn}}, 0)$ is marked with a cross.

which relate to self-intersections in Fig. 6(b,c). For example, the trajectory in Fig. 6(c) has self-intersections in the neighbourhood of the fixed points $(\rho_1, 0)$ and $(\rho_{\mathrm{B}}, 0)$, and these are not consistent with the second order dynamics, (18,19,20) and (18,19,21) respectively, that should hold at these points. The inescapable conclusion is that the PDE system (14,15) is unable to describe these effects, and a higher order model, perhaps a higher order PDE, is required.

The shortcomings of the second order theory are immediate when one considers the linearisation of heavy traffic fixed points $(X, 0)$ for which $X > \rho_{\max}$. As shown above, these are either stable nodes or spirals (and hence have no unstable directions). Consequently, solution profiles may relax on to such plateaus in the increasing x direction, but have no subsequent means of escape. However in our set-up, escape is forced by the boundary conditions, and hence second order theory must fail.

6 Discrete Spectral Analysis

The goal now is to explain how the discrete model phase-plane trajectories escape from the fixed points in heavy traffic, since we have shown that this behaviour cannot be replicated by (18,19). In Fig. 6, one can see that the heavy traffic fixed points ($(\rho_2, 0)$ in Fig. 6(b) and $(\rho_{\mathrm{B}}, 0)$ and $(\rho_1, 0)$ in Fig. 6(c)) have a complicated Shilnikov-type structure, which when projected into two dimensions results in self-intersections. It may well be possible to explain the structure of these fixed points by deriving PDE models which exploit higher order terms in the Taylor expansion of the discrete model, and hence include more dimensions of phase-space. However, the approach here is to analyse the

spectrum of the discrete problem (1,2) directly.

The first step is to use $\dot{h}_n = v_{n-1} - v_n$, and consequently $\ddot{h}_n = \dot{v}_{n-1} - \dot{v}_n$ to eliminate velocity and write (1,2) in terms of coupled second order ODEs

$$\frac{1}{\alpha}\ddot{h}_n + \dot{h}_n + \{V(h_n) - V(h_{n-1})\} = 0, \tag{25}$$

for the headway variables alone. In a travelling wave solution, each vehicle has the same motion as the one in front, but with a time delay of τ, which is given by the reciprocal of the flow rate in the stationary case that we consider here. Thus $h_{n-1}(t) = h_n(t+\tau)$, with

$$\tau = h_*/V(h_*) > 0, \tag{26}$$

reduces system (25) to the single advance equation

$$\frac{1}{\alpha}\ddot{h}(t) + \dot{h}(t) + \{V(h(t)) - V(h(t+\tau))\} = 0. \tag{27}$$

Our interest is in the near-equilibrium behaviour of (27), and so we write $h = h_* + \tilde{h}(t)$, $\tilde{h}(t)$ small, and linearise to find

$$\frac{1}{\alpha}\ddot{\tilde{h}} + \dot{\tilde{h}} + V'(h_*)\left\{\tilde{h} - \tilde{h}(t+\tau)\right\} = 0, \tag{28}$$

which we solve with the exponential ansatz $\tilde{h} = \mathrm{re}\left(A\mathrm{e}^{\lambda t}\right)$, where A is real and λ is generally complex. This yields the characteristic equation

$$\frac{1}{\alpha}\lambda^2 + \lambda + V'(h_*)\left\{1 - \mathrm{e}^{\tau\lambda}\right\} = 0. \tag{29}$$

This type of mixed polynomial / exponential equation has received much attention in the past, see e.g. [14]. In contrast to the second order dynamics of (18,19), Eq. (29) has infinitely many roots, and Fig. 9 displays numerical solutions for representative parameter values. In each case the spectrum consists of a pair of eigenvalues which correspond to those of the PDE analysis, zero, and an open 'fan' of complex conjugate pairs in the right-hand complex plane. Thus in Fig. 9(b,c), the complex conjugate pairs which are highlighted in bold describe the oscillatory escape from heavy traffic plateaus shown in Fig. 1(b,c).

Since Fig. 9 is based on numerical solution techniques, the remaining challenge is to prove that it is representative of all possible scenarios and that no

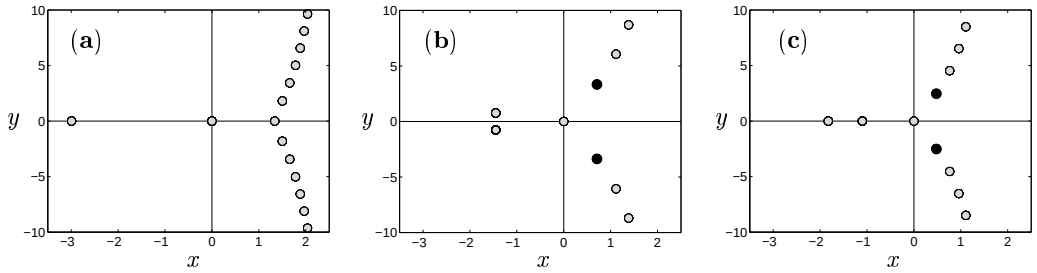

Fig. 9. The markers in (a-c) denote solutions $\lambda = \psi + \mathrm{i}\omega$ to (29). In panels (a-c), parameters are chosen such that the spectrum calculated represents respectively: the light traffic bottleneck plateau, as in Fig. 1(a); the medium density plateau just upstream of the bottleneck, as in Fig. 1(b); and the high density plateau outside of the bottleneck, as in Fig. 1(c). The complex conjugate pairs marked in bold in panels (b,c) are those that explain oscillatory x-increasing escape from heavy traffic.

other balance of eigenvalues between the left-hand and right-hand half-plane is possible. This analysis has three stages:

(1) We show that for $\alpha > 2V'(h_*)$, purely imaginary solutions $\lambda = \mathrm{i}\omega$, with $\omega \neq 0$, are impossible. Since solutions λ are continuous in problem parameters, spectrum may only cross from left to right half-planes or vice-versa by passing through the origin.
(2) Consequently, we find conditions for small solutions λ by using Taylor expansions, and we show that spectrum may only cross the origin when we move between light and heavy traffic cases, i.e. when h^* passes through $\rho_{\max}$. Thus the number of solutions in the left-hand half-plane may be completely characterised by considering a single light traffic and a single heavy traffic case.
(3) We thus focus on the special case $\alpha > 4V'(h_*)$ for which the spectrum may be shown to lie on loci of especially simple form. This procedure allows us to bound left-hand half-plane spectrum and to characterise the open 'fan' of eigenvalues in the right-hand half-plane. Since the spectrum does not cross the imaginary axis as we change α provided that we maintain $\alpha > 2V'(h_*)$, this argument establishes that Fig. 9(a-c) is representative.

Part 1. We substitute $\lambda = \mathrm{i}\omega$, ω real, in (29) and separate real and imaginary parts. Algebraic terms in ω may be eliminated and we may divide through by a factor of non-zero ω to obtain

$$\frac{\alpha}{V'(h_*)} = \frac{\sin^2 \omega\tau}{1 - \cos \omega\tau}. \tag{30}$$

We then expand the trigonometric terms using half-angle formulae to show that (30) has no solutions for $\alpha > 2\mathrm{maxV}'(\mathrm{h}_*)$. Note that (30) is equivalent to the neutral stability boundary derived by Bando et al [6].

Part 2. We consider the spectrum λ in the neighbourhood of the origin by expanding the characteristic equation (29) to $O(\lambda^2)$ to obtain

$$\lambda \left[\left(\frac{1}{\alpha} - \frac{\tau^2 V'(h_*)}{2} \right) \lambda + (1 - \tau V'(h_*)) \right] = 0, \tag{31}$$

which yields

$$\lambda = 2\alpha \left(\frac{1 - \tau V'(h_*)}{2 - \alpha \tau^2 V'(h_*)} \right), \tag{32}$$

for the small non-zero root which passes through the origin at

$$\tau V'(h_*) = \frac{h_* V'(h_*)}{V(h_*)} = 1. \tag{33}$$

By using $\hat{V}(\rho) := V(1/\rho)$ and $Q(\rho) := \rho \hat{V}(\rho)$, one may show that (33) corresponds to $Q'(\rho) = 0$, i.e., the boundary between light and heavy traffic. Moreover Equation (32) is in asymptotic agreement with the small root of the PDE model spectrum, since a small eigenvalue $\hat{\lambda}$ expansion of the Jacobian (22) may be mapped directly onto (32) via the transformation $h_* = 1/X_*$, observing that $\lambda = \hat{V}(X_*)\hat{\lambda}$.

Part 3. We now sketch an analysis in the full complex plane, by writing (29) in the form

$$h(\lambda) = f(\lambda) - g(\lambda) = 0, \tag{34}$$

where

$$f(\lambda) = \frac{1}{\alpha}\lambda^2 + \lambda + V'(h_*) \quad \text{and} \quad g(\lambda) = V'(h_*)\mathrm{e}^{\tau\lambda}. \tag{35}$$

Solutions must necessarily lie on the loci of $|f(\lambda)| = |g(\lambda)|$. Hence by writing $\lambda = \psi + \mathrm{i}\omega$, where ψ and ω are real, we find

$$\omega^2 = -p(\psi) \pm \sqrt{p(\psi)^2 + \alpha^2 \left(g(\psi)^2 - f(\psi)^2\right)}, \tag{36}$$

where

$$p(\psi) = \left(\psi + \frac{\alpha}{2} \right)^2 + \alpha \left(\frac{\alpha}{4} - V'(h_*) \right). \tag{37}$$

Thus for $\alpha > 4V'(h_*)$, we have $p(\psi) > 0$ for all ψ. Hence provided $f(\psi) < g(\psi)$, Eq. (36) has a single positive root for ω^2, and otherwise none. The characterisation of the loci $\omega = \omega(\psi)$ of $|f(\lambda)| = |g(\lambda)|$ is thus achieved via a bifurcation analysis of the real equation

$$f(\psi) = g(\psi), \tag{38}$$

whose solutions also yield real roots $\lambda = \psi$ of (29).

Firstly, note that $f(\psi) - g(\psi)$ is monotone decreasing for $\psi < -\alpha/2$, and that $f(-\alpha) - g(-\alpha) = V'(h_*) - V'(h_*)\mathrm{e}^{-\alpha\tau} > 0$ whereas $f(-\alpha/2) - g(-\alpha/2) = V'(h_*) - \alpha/4 - V'(h_*)\mathrm{e}^{\psi\alpha/2} < 0$. Hence there is a unique root $\psi_1 \in (-\alpha, -\alpha/2)$ to (38) and none further to the left. Next note that $\psi = 0$ is always a solution to (38). The remaining analysis breaks down into a consideration of the heavy traffic case, for which $f'(0) < g'(0)$, hence $f(0-) > g(0-)$, so that there is a consequently an additional root $\psi_2 \in (-\alpha/2, 0)$, and the light traffic case for which the additional root ψ_2 is positive.

An analysis of the pattern of sign changes of $f - g$ then yields the structure of the $|f| = |g|$ loci, which consists of a closed bounded curve in the left-hand half-plane, and an open curve in the right-hand half-plane which is attached to the positive real root in the light traffic case and to the origin in the heavy traffic case. Since f dominates g on any sufficiently large contour to the left of the open section of the locus, Rouché's theorem [15] proves that the solution count of (29) is the same as that of $f = 0$ to the left of this curve (i.e., two roots). Hence we establish that Fig. 9 has captured all the spectrum.

7 Conclusions

In this paper we have found and analysed interesting macroscopic wave structures that emerge in a simple microscopic traffic model with spatial heterogeneity. Because we posed the problem with periodic (i.e., ring-road) boundary conditions, there is a natural flow balance which leads to stationary density profiles consisting of sets of plateaus separated by sharp interfaces. In the infinite line (open road) setting, one would expect a more complicated outcome in which wave structures can propagate to infinity and this warrants further study, as do more general settings such as merges, lane drops, and moving bottlenecks.

Our overall approach has been multiscale, in that we have tried to understand the macroscopic solution profiles of an underlying microscopic model at four distinct levels of increasing sophistication but also of decreasing tractability:

(1) Basic flow and density balances (essentially the zeroth order model): This gives rise to algebraic equations with isolated but non-unique solutions for plateau values.
(2) First order conservation law (Lighthill-Whitham model): Characteristic methods impose uniqueness for plateau values but fronts are represented unrealistically by discontinuous shocks.
(3) Second order traffic models (of similar type to that of Kerner-Konhäuser [4], but derived [9,8] directly from the original microscopic model): Global dynamical systems arguments (phase-planes) explain qualitatively most interface structure but cannot explain the (increasing x) escape of trajectories from heavy traffic plateaus.
(4) Original microscopic traffic model: This analysis is only tractable at the linearised level but we show how the extra spectra can explain the oscillatory escape from heavy traffic plateaus.

As a general remark, we believe that in a spatially homogeneous setting, all solution features can be adequately described by second order continuum theory. Hence, the novelty in this paper is that the model discontinuity forces structures with such short length scales that the assumptions of the second order approximation break down, and consequently these features can only be analysed via the original microscopic model.

A relatively unexplored area that has emerged from this study is the analysis of global connections in the original (and exact) microscopic model, which is in essence a lattice differential equation. (We emphasise again that in this paper, the microscopic model is analysed only at the linear level.) Hence there is future scope for a formal bifurcation analysis of the advance equation (27).

References

[1] D. Chowdhury, L. Santen, A. Schadschneider, Statistical physics of vehicular traffic and some related systems, Phys. Reports 329 (2000) 199–329.

[2] B. Kerner, The Physics of Traffic, Springer-Verlag, 2004.

[3] D. Helbing, Traffic and related self-driven many-particle systems, Rev. Mod. Phys. 73 (4) (2001) 1067–1141.

[4] B. S. Kerner, P. Konhäuser, Cluster effect in initially homogeneous traffic flow, Phys. Rev. E 48 (4) (1993) R2335–R2338.

[5] G. Whitham, Linear and Nonlinear Waves, John Wiley and Sons, New York, 1974.

[6] M. Bando, K. Hasebe, A. Nakayama, A. Shibata, Y. Sugiyama, Dynamical model of traffic congestion and numerical simulation, Phys Rev. E 51 (2) (1995) 1035–1042.

[7] H. Hanaura, T. Nagatani, K. Tanaka, Jam formation in traffic flow on a highway with some slowdown sections, Physica A 374 (2007) 419–430.

[8] H. K. Lee, H.-W. Lee, D. Kim, Macroscopic traffic models from microscopic car-following models, Phys. Rev. E 64 (5) (2001) 056126.

[9] P. Berg, A. Mason, A. Woods, Continuum approach to car-following models, Phys. Rev. E 61 (2) (2000) 1056–1066.

[10] J. Ward, R. Wilson, B. P., Wave selection problems in the presence of a bottleneck, in: A. Schadschneider, T. Pöschel, R. Kühne, M. Schreckenberg, D. Wolf (Eds.), Traffic and Granular Flow '05, Springer-Verlag, 2007, pp. 565–576.

[11] W. L. Jin, H. Zhang, The inhomogeneous kinematic wave traffic flow model as a resonant nonlinear system, Trans. Sci. 37 (3) (2003) 294–311.

[12] R. Wilson, P. Berg, Existence and classification of travelling wave solutions to second order highway traffic models, in: M. Fukui, Y. Sugiyama, M. Schreckenberg, D. Wolf (Eds.), Traffic and Granular Flow '01, Springer-Verlag, 2003, pp. 85–90.

[13] Y. Kuznetsov, Elements of Applied Bifurcation Theory, Springer-Verlag, 1995.

[14] K. Cooke, P. van den Driessche, On zeroes of some transcendental equations, Funkcialaj Ekvacioj 29 (1986) 77–90.

[15] W. Rudin, Real and Complex Analysis, McGraw-Hill, 1960.